

Semiconductor color-center structure and excitation spectra: Equation-of-motion coupled-cluster description of vacancy and transition-metal defect photoluminescence

Jesse J. Lutz*

ORISE fellow residing at Air Force Institute of Technology, Wright-Patterson Air Force Base, Ohio 45433, USA

Xiaofeng F. Duan

Air Force Research Laboratory DoD Supercomputing Resource Center, Wright-Patterson Air Force Base, Ohio 45433, USA

Larry W. Burggraf

Air Force Institute of Technology, Wright-Patterson Air Force Base, Ohio 45433, USA

(Received 28 September 2017; published 5 March 2018)

Valence excitation spectra are computed for **deep-center silicon-vacancy defects in 3C, 4H, and 6H silicon carbide (SiC)**, and comparisons are made with literature photoluminescence measurements. Optimizations of nuclear geometries surrounding the defect centers are performed within a Gaussian basis-set framework using many-body perturbation theory or density functional theory (DFT) methods, with computational expenses minimized by a QM/MM technique called SIMOMM. Vertical excitation energies are subsequently obtained by applying excitation-energy, electron-attached, and ionized equation-of-motion coupled-cluster (EOMCC) methods, where appropriate, as well as time-dependent (TD) DFT, to small models including only a few atoms adjacent to the defect center. We consider the relative quality of various EOMCC and TD-DFT methods for (i) energy-ordering potential ground states differing incrementally in charge and multiplicity, (ii) accurately reproducing experimentally measured photoluminescence peaks, and (iii) energy-ordering defects of different types occurring within a given polytype. The extensibility of this approach to transition-metal defects is also tested by applying it to silicon-substituted chromium defects in SiC and comparing with measurements. It is demonstrated that, when used in conjunction with SIMOMM-optimized geometries, EOMCC-based methods can provide a reliable prediction of the ground-state charge and multiplicity, while also giving a quantitative description of the photoluminescence spectra, accurate to within 0.1 eV of measurement for all cases considered.

DOI: [10.1103/PhysRevB.97.115108](https://doi.org/10.1103/PhysRevB.97.115108)

I. INTRODUCTION

Certain point defects in wide-band-gap semiconductors have been identified as promising candidates for use as qubits in quantum computing, communication, and sensing applications [1]. A well-known example is the nitrogen-vacancy (NV) color center in diamond, which harbors an anionic electronic structure $[(NV)^-]$ with well-defined $S = 1$ spin states that have been initialized and coherently manipulated using optical or microwave radiation [2]. The resulting stimulated emission, occurring between the 3A_2 ground state and the 3E excited state, produces a tunable photoluminescence, polarized according to an applied external magnetic field. The demonstration of long spin-coherence times at room temperature established $(NV)^-$ centers as one of the most stable, efficient, high-quality single-photon sources known [3–5]. However, diamond has inherent engineering limitations and, as a result, defects with similar properties are being eagerly sought out, both in other solid-state materials [6] and in nano-materials [7].

The most closely related material to diamond in terms of sp^3 bonding is silicon carbide (SiC), and its anionic silicon-vacancy (V_{Si}^-) defects are arguably better qubit candidates than

the diamond $(NV)^-$ defect. The SiC V_{Si}^- defects, characterized by a $^4A_2 \rightarrow ^4E$ transition [8], have several superior properties: They exhibit no luminescence intermittency or blinking [5,9], they are a half-integer $S = \frac{3}{2}$ spin (thus Kramers theorem holds) [10,11], and they are intrinsic defects, which do not require doping and can therefore be more easily created (e.g., using a transmission electron microscope [12], a focused ion beam [13], ion implantation [14], etc.), as reported in Ref. [15], where a scalable array of single silicon vacancy centers was realized [15]. Furthermore, the bulk material properties of SiC make it more amenable than diamond to high-voltage, high-power, and high-temperature applications and it is also more promising as a long-term candidate material due to its physical durability [16], engineering flexibility [17], and increasingly inexpensive manufacturing cost [18,19]. One disadvantage is that the optically detected magnetic resonance of V_{Si}^- SiC has a lower visibility compared to that of the $(NV)^-$ center in diamond, but this too is being overcome [20].

Diamond $(NV)^-$ and SiC V_{Si}^- defects emit in a region of the infrared which is nonideal for utilizing existing single-mode fiber-optic infrastructure. Recent telecommunications systems use wavelength-division multiplexing, which can use the full range of wavelengths between 1260 and 1670 nm (or 0.74 and 0.98 eV), and other popular multimode and single-mode fiber implementations operate using wavelengths of 850, 1300, and

*jesse.lutz.ctr@afit.edu

1550 nm (or 0.80, 0.95, and 1.46 eV), with the latter being associated with the transmission-optimal so-called C band [21]. Consequently, several other common SiC defects are also under consideration, including the neutral divacancy [3,22], nitrogen vacancies [23,24], and antisite vacancies [25,26]. More promising still is the prospect of doping with transition- or heavy-metal elements [27], although it is unclear at the outset which implants will emit the desired wavelengths.

Difficulties are often encountered when using spectroscopic techniques to distinguish between different types of vacancies or screen for specific properties across a series of substitutional defects. This presents a great opportunity for computational modeling. Modeling photoluminescence spectra requires determination of the nuclear geometry of the solid-state defect, followed by generation of accurate energy differences between the ground and excited states. Acceptable geometries can often be obtained for weakly correlated materials using density functional theory (DFT) methods in a plane-wave basis, and its computational scaling, usually \mathcal{N}^3 – \mathcal{N}^4 with the system size \mathcal{N} , offers a relatively inexpensive framework. Unfortunately, problems arise when extending DFT to excited states through the time-dependent (TD) DFT formalism (see, e.g., Refs. [28–32] for reviews). Alternatively, studies conducted in a plane-wave basis may apply the many-body *GW* approximation [33], sometimes even in conjunction with DFT-optimized structures [34], in order to gain access to band structure or excited states. The *GW* approximation provides much more accurate results, but it also has well-known fundamental limitations: To name a few, it suffers from self-consistency errors, and the route toward an exact theory is unclear.

Quantum chemistry methods offer one path towards an exact description of electronic wave functions in real solids [35], and among the most accurate general-purpose *ab initio* methods available are those based on the single-reference coupled-cluster (SRCC) theory for ground states and its equation-of-motion (EOM) CC extension to excited states. These methods are size consistent and systematically improvable, but, despite recent progress toward reducing the expense of band-structure SRCC/EOMCC implementations [36,37], their computational scaling remains intractable for complex crystalline solids. An acceptable alternative for geometry optimizations is provided by the related second-order Möller Plesset many-body perturbation theory (MP2), which has a noniterative \mathcal{N}^5 scaling, but for an accurate treatment of excitation energies EOMCC-based methods are needed. The most basic EOMCC methods, including only single and double excitations, require steep iterative \mathcal{N}^5 – \mathcal{N}^6 scalings, and this makes treatment of even a single unit cell very taxing in terms of the required CPU cycles. Meanwhile explicit treatment of a supercell model with Gaussian-based *ab initio* methods will be impossible for many years to come, even with modernized codes.

Here a twofold strategy is used to minimize the computational expense associated with the aforementioned accurate computational methodologies. The first step is to partition the geometry optimization into a small group of atoms significantly perturbed by introduction of the defect site, and a comparatively very large group of atoms whose environment is unchanged by introduction of the defect. The

former will be treated using high-level quantum-mechanical (QM) methods, while the latter will be treated using low-level molecular-mechanical (MM) methods. The second step is to exploit the highly-localized nature of the associated defect photoluminescence by applying accurate excited-state many-body methods to small model systems, e.g., only those few atoms directly adjacent to the defect. For over 50 years the local nature of excitations in defect solids has been used to develop approximate methods in which the total system is subdivided into a defect subspace and a complementary crystalline region, so this is not a novel proposition [38].

The first step is realized by utilizing the surface integrated molecular-orbital molecular-mechanics (SIMOMM) method of Shoemaker *et al.* [39], which falls into the general class of QM/MM hybrid methods. The SIMOMM framework imposes a less rigid treatment of the capping atoms than its predecessor, the IMOMM model of Maseras and Morokuma [40], and this reduces artificial strain imposed on the QM structure. SIMOMM was originally developed for the study of surface chemical systems, and by now its utility has been proven repeatedly for describing chemistry on Si and SiC surfaces [41–50]. SIMOMM geometry optimizations are performed under the Born-Oppenheimer approximation, which in this case is based on extremely robust assumptions [51]. The current study is the first attempt at applying SIMOMM to describe nuclear geometries of deep-center defects in semiconductors. Note that for defects in ionic or metallic solids other, more appropriate, QM/MM methods exist (see, e.g., Refs. [52–54]).

The second step of the above-mentioned procedure is also very challenging due to the nature of the electronic excitations of interest. Excitation energies of open-shell systems with high spacial symmetry are notoriously difficult to describe, and, as a result, we employ the electron-attached (EA) and ionized (IP) EOMCC methods [55,56]. These methods have been shown to be particularly accurate for describing both ground and excited states of odd-electron, open-shell molecules. In these schemes the $(N \pm 1)$ -electron systems of interest are formed through application of an electron-attaching or ionizing operator to the correlated ground-state reference of a related N -electron system, obtained using the SRCC approach. Alternatively, if even-electron, open-shell states are desired, they can be described by the excitation-energy (EE) EOMCC method, where the usual particle-conserving operator is applied to the same correlated N -electron reference. This framework allows for orthogonally spin-adapted and systematically improvable calculations of the ground and excited states of N - and $(N \pm 1)$ -electron systems mutually related by an N -electron correlated reference function.

Electronically excited states dominated by one-electron transitions, particularly those that correspond to one-electron transitions from nondegenerate doubly-occupied molecular orbitals (MOs) to a singly-occupied molecular orbital (SOMO), can be accurately described by the basic EE-, EA-, or IP-EOMCCSD approaches. Meanwhile, electronic transitions characterized by two- or other, more complicated, many-electron processes, require higher-than-double excitations in order to obtain reliable results. The expense of such calculations usually limits their applicability to the smallest systems, but larger systems can be efficiently treated using the active-space EE-, EA-, and IP-EOMCC variants [57–60], such as

those including active-space triples, i.e., EE-, EA-, and IP-EOMCCSDt [61,62]. Here a strategically-chosen small subset of orbitals is considered that captures the largest contributions from triple excitations.

The performance of both the basic EE-, EA-, and IP-EOMCCSD methods and the active-space EA- and IP-EOMCCSDt approaches are tested here for their ability to describe solid-state SiC defect excitation spectra. The active-space methods have already been applied to small open-shell molecules [61–63] and ionic transition-metal complexes [64], where it was demonstrated that they can provide an accurate treatment as compared to calculations employing a full treatment of triple excitations. The current study is the first application to deep-center defects, where the resulting EOMCC excitation energies can be directly compared to photoluminescence measurements. Some TD-DFT calculations are included for comparison, but benchmarking various functionals is outside of the scope of this work so we use those deemed optimal for Si_nC_m ($n, m \leq 12$) molecules in Refs. [65] and [66] (see Sec. III for further details).

The goal of the present work is to develop a systematically improvable procedure for describing defect excitation spectra, and we use as benchmarks the available photoluminescence spectra for the V_{Si}^- defects in 4H- and 6H-SiC [67] and also the chromium silicon-substitutional defect in SiC [27]. Two distinct Si-vacancy sites exist in 4H-SiC, the k site and the h site [67], and each exhibit distinct signature photoluminescence peaks in the infrared. Meanwhile, three distinct sites exist in 6H-SiC, the $k1$, $k2$, and h sites [67], each of which also emit in the infrared. The V_{Si}^- defect in 3C-SiC has not been widely reported as it potentially undergoes low-temperature annealing [68,69], but there is evidence it lies in the same range as V_{Si}^- defects in the other polytypes (1.3–1.4 eV) [70]. The measured emission frequencies of each of these six defects all fall within 0.1 eV of one another, but selective resonant optical excitation is still possible, as the spectral linewidths can be as small as 2 μeV [71]. A useful level of theory will be able to predict each frequency to an accuracy within 0.1 eV, while also giving the correct qualitative energy ordering of closely-spaced emission frequencies.

The structure of this paper is as follows: In Sec. II the basic theory of the EOMCC methods is presented, while in Sec. III specific details are given about how the computations were performed. Section IV reports investigations of SIMOMM convergence, qualitative and quantitative energy ordering of states with incremental changes in charge and multiplicity, and comparison of computed excitation energies with photoluminescence measurements for various defect sites. Conclusions and directions for future research are discussed in Sec. V.

II. THEORY

In this section we provide an overview of the EOM-CC methods used to describe the excitation energies of the SiC color centers. The EE-, EA-, and IP-EOMCC theories will be employed to consider relative energies of ground and excited states with varying charge and multiplicity. These EOMCC-based methods have several advantages over standard DFT and TD-DFT: They produce spin-adapted odd-electron states, they are systematically improvable, and they can be used to generate

N - and $(N \pm 1)$ -electron states of various multiplicities from a common correlated N -electron reference wave function.

In general, a wave function $|\Psi_\mu\rangle$, corresponding to state μ of interest, is expressed by applying a linear excitation operator R_μ to the ground-state SRCC wave function,

$$|\Psi_\mu\rangle = R_\mu |\Psi_0^{(N)}\rangle, \quad (1)$$

where $|\Psi_0\rangle = e^T |\Phi\rangle$ is the CC ground state wave function formulated from the many-body cluster operator T and $|\Phi\rangle$ is for the EOMCC methods in this work always given by the restricted Hartree-Fock (RHF) wave function, $|\Phi\rangle = |\Phi^{\text{RHF}}\rangle$. By choosing as a starting point an N -electron reference CC function, $|\Psi_0^{(N)}\rangle$, we are able to maintain commutation relations with the S^2 and S_z operators throughout. To access both N - and $(N \pm 1)$ -electron states, the linear excitation operator R_μ must be either particle-conserving, $R_\mu = R_\mu^{(N)}$, or particle-nonconserving, $R_\mu = R_\mu^{(N \pm 1)}$, respectively, for the resulting state to be a spin eigenfunction of the Hamiltonian.

In the particle-conserving EE-EOMCC theory, excited state energies and wave functions are obtained for an N -electron system by applying in Eq. (1) a linear excitation operator $R_\mu^{(N)}$ of the form

$$\begin{aligned} R_\mu^{(N)} &= R_{\mu,0} + R_{\mu,1} + R_{\mu,2} + \dots \\ &= r_{\mu,0} + \sum_a r_a^i a^i a_i + \sum_{ab} r_{ab}^{ij} a^i a^j a_b a_a + \dots, \end{aligned} \quad (2)$$

where $i, j, \dots (a, b, \dots)$ are the occupied (unoccupied) orbitals in $|\Psi_0^{(N)}\rangle$, $a^p(a_p)$ are the creation (annihilation) operators associated with the spin-orbital basis set $|p\rangle$ used in the calculations, and $r_a^i, r_{ab}^{ij}, \dots$ are the excitation amplitudes defining the many-body components of $R_\mu^{(N)}$, determined by diagonalizing the similarity-transformed Hamiltonian $\bar{H} = e^{-T^{(N)}} H e^{T^{(N)}}$ resulting from the ground-state N -electron CC calculations.

In the particle-nonconserving EA- and IP-EOMCC approaches, ground- and excited-state wave functions are obtained corresponding to states with $(N - 1)$ - or $(N + 1)$ -electron open-shell systems, respectively. The corresponding electron-attaching and ionizing operators, $R_\mu^{(N+1)}$ and $R_\mu^{(N-1)}$, respectively, entering Eq. (1) are defined as

$$\begin{aligned} R_\mu^{(N+1)} &= R_{\mu,1p} + R_{\mu,2p-1h} + R_{\mu,3p-2h} + \dots \\ &= \sum_a r_a a^a + \sum_{a < b} r_{ab}^j a^j a^a a_b \\ &\quad + \sum_{\substack{a < b < c \\ j > k}} r_{abc}^{jk} a^j a^k a^a a_b a_c a_j + \dots \end{aligned} \quad (3)$$

and

$$\begin{aligned} R_\mu^{(N-1)} &= R_{\mu,1h} + R_{\mu,2h-1p} + R_{\mu,3h-2p} + \dots \\ &= \sum_a r_a^i a_i + \sum_{\substack{i > j \\ b}} r_b^{ij} a^i a^j a_b a_i \\ &\quad + \sum_{\substack{i > j > k \\ b < c}} r_{bc}^{ijk} a^i a^j a^k a^b a_c a_k a_j a_i + \dots, \end{aligned} \quad (4)$$

where $r^i, r_b^{ij}, r_{bc}^{ijk}, \dots$ and $r_a, r_{ab}^j, r_{abc}^{jk}, \dots$ are the corresponding electron-attaching or ionizing amplitudes defining the relevant $1h, 2h-1p, 3h-2p, \dots$ or $1p, 2p-1h, 3p-2h, \dots$ components of $R_\mu^{(N-1)}$ and $R_\mu^{(N+1)}$, respectively, determined by diagonalizing the similarity transformed Hamiltonian in the appropriate sector of the Fock space.

Active-space approaches represent a practical way to account for higher-than-doubly excited clusters in the CC and EOMCC equations [57–60,72]. The idea is to subpartition the one-electron basis of occupied and unoccupied spin orbitals into (i) core or inactive occupied spin orbitals, designated as $\mathbf{i}, \mathbf{j}, \dots$, (ii) active occupied spin orbitals, designated as $\mathbf{I}, \mathbf{J}, \dots$, (iii) active unoccupied spin orbitals, designated as $\mathbf{A}, \mathbf{B}, \dots$, and (iv) virtual or inactive unoccupied spin orbitals, designated as $\mathbf{a}, \mathbf{b}, \dots$. After dividing the available orbitals into one of these four categories, only active orbitals are used to define the active-space component of the EE, EA, or IP operators $R_\mu^{(N)}$, $R_\mu^{(N+1)}$, or $R_\mu^{(N-1)}$, respectively. As an example, the active-space EA-EOMCCSDt $\{N_u\}$ approach using N_u active unoccupied orbitals is obtained by replacing the $3p-2h$ component $R_{\mu,3p-2h}$ of the electron attaching operator $R_\mu^{(N+1)}$, Eq. (4), by

$$r_{\mu,3p-2h} = \sum_{\substack{j > k \\ \mathbf{A} < \mathbf{b} < \mathbf{c}}} r_{\mathbf{A}bc}^{jk} a^{\mathbf{A}} b^{\mathbf{a}} c^{\mathbf{a}} a_k a_j. \quad (5)$$

Assuming a small active space is chosen, there will be relatively few amplitudes $r_{\mathbf{A}bc}^{jk}$ defining $r_{\mu,3p-2h}$ in Eq. (5), and they will not be much more expensive to compute than the remaining $1p$ and $2p-1h$ amplitudes r_a and r_{ab}^j that enter the $(N+1)$ -electron wave functions of the active-space EA-EOMCCSDt $\{N_u\}$ approach. The IP-EOMCCSDt $\{N_o\}$ active-space method is formulated in an analogous way.

III. COMPUTATIONAL DETAILS

Here we outline necessary details for the calculations reported in Sec. IV. Supercells with perfect lattice geometries were generated using the VESTA package [73]. Perimeter C atoms were capped with hydrogens and Si atoms were capped with CH_3 groups, as H atoms and CH_3 groups have very similar electronegativities of 2.2 and 2.3, respectively [74]. Defect sites were embedded into the cluster models using Avagadro and Avagadro 2 [75]. The resulting geometries were converted to the proper format for the Tinker package [76] using OpenBabel [77] and for the GAMESS package [78,79] using MacMolPlt [80].

Geometry optimizations are accelerated significantly by parallel implementations leveraging analytic gradients. In a previous study we have investigated the relative performance of a variety of DFT, MP2, and high-level CC methods for producing geometries of several Si_nC_m ($n \leq m \leq 12$) molecules [65], which are expected to exhibit similar many-body physics to defects in solid-state SiC. The previous study found that MP2 and DFT with the M11 functional were good alternatives, which could closely reproduce the geometries predicted by high-level SRCC methods. Since it is known in advance that the V_{Si}^- defects have $^4\text{A}_1$ ground state, unrestricted (U) self-consistent field variants were employed where appropriate, i.e., UMP2 and UM11. Unlike the open-shell coupled-cluster codes, both

the UMP2 and UM11 methods have parallel analytic gradients implemented in GAMESS [81], and consequently they are used here for the QM portion of optimizations. Restricted open-shell HF (ROHF) references were also tested, but convergence problems were encountered. Optimizations of excited states were not performed since it has been shown that Stoke's shifts for V_{Si}^- defects remain on the order of 10 meV [82].

The T_d (C_{6v}) symmetry of bulk 3C- (4H- and 6H-) SiC are lowered to C_{3v} in the presence of vacancy defects such as V_{Si}^- . Unfortunately, the SIMOMM approach does not currently utilize the spacial symmetry of Abelian groups, as is otherwise fully implemented in GAMESS. The SIMOMM-optimized structures reported here retained an approximate C_{3v} symmetry, but to facilitate comparisons with other results found in the literature we had to trace back C_{3v} orbital labelings. Due to the lowered symmetry, an otherwise degenerate E excited state in C_{3v} symmetry had slightly different energies; in such cases we report the average of the two energy levels, which usually differed by a small amount (in many cases 1–5 meV). Consequently, all reported energy values are rounded to the nearest 0.01 eV, except when more decimals are needed for qualitative discussions.

Excited-state calculations were performed using the EOMCC and TD-DFT approaches. The B3LYP functional was chosen since it performed particularly well for Si_nC_m ($n, m \leq 12$) clusters in Refs. [66] and [83]. For TD-DFT calculations of open-shell species, only unrestricted (U) Kohn-Sham (KS) determinants were employed, as it has been advocated by Pople, Gill, and Handy that ROHF KS determinants should be avoided whenever possible [84]. These methods were applied to SIMOMM-optimized geometries including only the four carbon atoms immediately surrounding the defect with three capping hydrogen atoms each. Ground states are labeled with an X, while roman numerals label excited states of each symmetry, starting with 1. All computed excitation energies reported here are vertical, which is expected to be a good approximation for solid-state photoluminescence phenomena. Stoke's shifts for V_{Si}^- have been measured and are expected to be very small, on the order of 10 meV [82].

For EA-EOMCCSDt calculations on the V_{Si}^- defect, a neutral CCSD reference [Fig. 1(a)] was used with active-space orbitals chosen as 5e and 15a₁ in order to construct the corresponding quartet state [Fig. 1(d)]. For the IP-EOMCCSDt calculations a doubly-anionic reference [Fig. 1(b)] was used with active-space orbitals chosen as 4e, 5e, 12a₁, and 13a₁ in order to construct the corresponding quartet state [Fig. 1(d)].

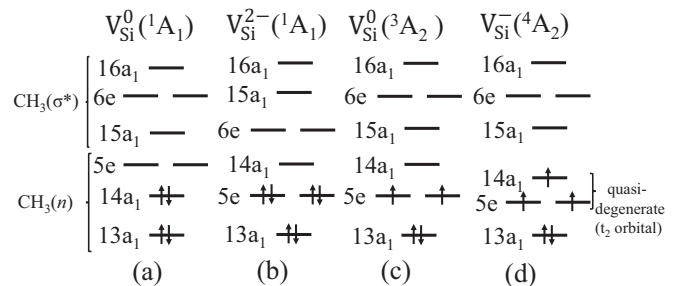


FIG. 1. Single-particle representations of several potential ground states for V_{Si} and their qualitative valence-orbital energy-orderings and occupations.

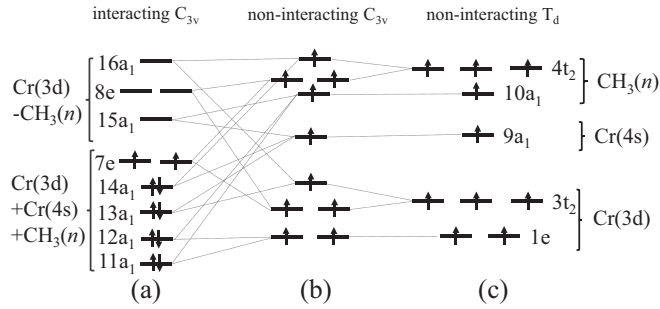


FIG. 2. Schematic representation of the valence orbital energy levels for $\text{Cr}(\text{CH}_3)_4$ assuming C_{3v} and T_d symmetries with the former also considered with and without orbital mixing.

Tests including more active-space orbitals did not have a significant effect on the excitation energies of interest. The EE-EOMCCSDt method is not currently available in GAMESS, so all EE-EOMCC calculations include singles and doubles only. For EE-EOM-CCSD calculations a neutral CCSD reference [Fig. 1(a)] was used in order to construct the corresponding triplet state [Fig. 1(c)].

When transition-metal silicon-substitutional defects are considered, the MO structure changes significantly as compared with the V_{Si} -type defects. As an example, the MOs of the chromium defect system are shown in Fig. 2. Starting from a T_d geometry in the noninteracting limit [Fig. 2(c)], an optimization will distort to a C_{3v} symmetry [Fig. 2(b)], while also hybridizing the Cr and CH_3 valence orbitals [Fig. 2(a)]. It can be seen that for the initial T_d geometry [Fig. 2(c)], when an optimization is performed on the neutral $^0\text{Cr}^0$ species all of the SOMOs can simply become doubly occupied Cr d orbitals, and, in practice, this electronic configuration does not always facilitate the required orbital mixing needed for the optimization to proceed. For this reason we chose instead the $^4\text{Cr}^{3+}$ state, which starts the optimization engaging the $3t_2$ orbitals symmetrically. Introducing the charge draws in the CH_3 dangling bonds and initiates orbital mixing, while the quartet open-shell system can still be easily described using a single Slater determinant.

In all QM calculations core orbitals were kept frozen, no molecular symmetry was enforced, and a spherical harmonic basis was used. For the SIMOMM optimizations, the MM partition was always treated using MM2 parameters [85], and the default maximum nuclear gradient convergence threshold was loosened to 1×10^{-3} Hartree/Bohr, since this was shown to have a relatively small effect on the final excitation energies while reducing the number of iterations considerably. DFT and TD-DFT calculations were performed in GAMESS using a very tight grid (JANS=2).

We utilize Pople's 6-31G, 6-31G*, and 6-31+G* basis sets [86–90] and Dunning's correlation-consistent cc-pVXZ and aug-cc-pVXZ basis sets [91–93], where X is the cardinal number of the basis set ($X = \text{D, T, Q, ...}$). Here cc-pVXZ and aug-cc-pVXZ are abbreviated as CCX and ACCX, respectively. For vacancy defect calculations ghost functions were also included to improve basis set convergence. These consisted of Si functions in the specified basis set and were placed at the vacancy-defect site.

IV. RESULTS AND DISCUSSION

The primary goal of this paper is to propose and validate Gaussian-based approaches for generating high-accuracy ground- and excited-state properties and energetics of vacancy and substitutional defects in semiconductors. While the procedures explored here are, in principle, systematically improvable to the exact solution, the steep computational scaling of the most accurate methods limits the scope of their application. Fortunately, photoluminescence spectra are available for benchmarking new methods and this facilitates convergence tests. Much of this study is thus devoted to identifying for use in future studies those levels of theory that offer a good compromise between accuracy and computational cost.

A. Defect geometry convergence using SIMOMM

As this is the first application of SIMOMM to deep-center defects, it is important to begin by testing whether the resulting geometrical parameters converge with increasing model size. Starting from a bulk model with perfect crystal coordinates, introduction of a point defect followed by optimization with SIMOMM causes the atoms directly adjacent to the defect site to break symmetry, as Jahn-Teller distortion elongates the primary symmetry axis [94]. A good single quantity to monitor for convergence is thus the average distance between the defect position and the four surrounding atoms, or \bar{R} . The 4H-SiC polytype was chosen for these tests because, unlike 3C-SiC, it has an anisotropic unit cell, and, unlike 6H-SiC, 4H-SiC is not too large to consider multiple concentric supercell dimensions (in integer-unit increments). While the exact geometrical structure has not been measured, prior plane-wave DFT calculations placed \bar{R} close to 2.0 Å [8]. A desirable level for a convergence threshold is then a distance $\Delta\bar{R} < 0.1$ Å, corresponding to $\Delta\bar{R} < 5.0\%$ in this case.

Table I collects \bar{R} values resulting from optimizations performed using various supercell sizes, QM model sizes, and levels of theory. When the QM model was treated at the UMP2/STO-3G level of theory with an adequate bulk MM model supercell of 128 unit cells ($8 \times 8 \times 2$), a rather large QM model size of $\text{C}_4\text{Si}_{12}\text{H}_{36}$ [Fig. 3(b)] was required before reaching the desired 5% convergence. Since the 252-electron $\text{C}_4\text{Si}_{12}\text{H}_{36}$ QM model would be computationally intractable for many accurate QM theories, this motivated us to investigate the effect of increasing the basis set size. Switching from the STO-3G to the CCD basis set improved convergence with the QM model size, and it was found that, when used with the $8 \times 8 \times 2$ supercell, the smallest 60-electron C_4H_{12} QM model [Fig. 3(a)], produced a \bar{R} value in agreement to within 5% with the best \bar{R} values reported here and in Ref. [8]. The $8 \times 8 \times 2/\text{C}_4\text{H}_{12}$ model treated at the UMP2/CCD level of theory represents the best compromise of model sizes we tested for 4H-SiC.

When a larger number of atoms are required in the QM model, DFT methods can also be used in conjunction with SIMOMM optimizations. For 4H-SiC, when the M11 functional was used in conjunction with the CCD basis set, an $8 \times 8 \times 2$ supercell, and the $\text{C}_4\text{Si}_{12}\text{H}_{36}$ QM model, SIMOMM optimizations produced a \bar{R} value of 2.007 Å. This value is in agreement to within 5% of our best UMP2/STO-3G result,

TABLE I. Average distances (\bar{R}) between the h center 4H-SiC V_{Si}^- defect and the four surrounding atoms, with convergence of the % difference observed for various aspects of the SIMOMM model.

| SIMOMM model specifications | | | | $\Delta \bar{R}$ (% difference) ^a | | |
|-----------------------------|-----------|---|---------------|--|----------|-----------|
| method | supercell | QM model | \bar{R} (Å) | QM model | MM model | basis set |
| UMP2/STO-3G | None | C ₄ H ₁₂ | 1.814 | | | |
| UMP2/STO-3G | None | C ₄₀ Si ₁₂ H ₁₂₀ | 2.321 | 5.9 | | |
| UMP2/STO-3G | 4×4×1 | C ₄ H ₁₂ | 1.967 | | 8.1 | |
| UMP2/STO-3G | 4×4×1 | C ₄ Si ₁₂ H ₃₆ | 2.038 | 3.5 | 7.1 | |
| UMP2/STO-3G | 4×4×1 | C ₄₀ Si ₁₂ H ₁₂₀ | 2.076 | 1.9 | 11.1 | |
| UMP2/STO-3G | 8×8×2 | C ₄ H ₁₂ | 1.936 | | 1.6 | |
| UMP2/STO-3G | 8×8×2 | C ₄ Si ₁₂ H ₃₆ | 2.005 | 3.5 | 1.6 | |
| UMP2/STO-3G | 8×8×2 | C ₄₀ Si ₁₂ H ₁₂₀ | 2.040 | 1.7 | 1.8 | |
| UMP2/CCD | None | C ₄ H ₁₂ | 1.856 | | | 2.3 |
| UMP2/CCD | None | C ₄ Si ₁₂ H ₃₆ | 3.895 | 46.5 | | 56.1 |
| UMP2/CCD | 4×4×1 | C ₄ H ₁₂ | 2.013 | | 8.1 | 2.3 |
| UMP2/CCD | 4×4×1 | C ₄ Si ₁₂ H ₃₆ | 2.338 | 14.9 | 50.0 | 13.7 |
| UMP2/CCD | 8×8×2 | C ₄ H ₁₂ | 1.964 | | 2.5 | 1.4 |
| UMP2/CCD | 8×8×2 | C ₄ Si ₁₂ H ₃₆ | 1.985 | 1.1 | 16.3 | 1.0 |
| UM11/CCD | 8×8×2 | C ₄ Si ₁₂ H ₃₆ | 2.004 | | | |
| UB3LYP/CCD | 8×8×2 | C ₄ Si ₁₂ H ₃₆ | 2.077 | | | |
| PBE ^b | 6×6×2 | (all atoms) | 2.053 | | | |

^aQuantity computed as $\frac{|V_1 - V_2|}{(V_1 + V_2)} \times 100$ with V_1 the preceding table entry with an appropriate incrementally smaller model specification.

^bPlane-wave calculation reported in Ref. [8].

our best UMP2/CCD result, and the literature plane-wave PBE value. Another popular functional choice, UB3LYP, was also tested and found to give a higher \bar{R} value that was in good agreement with the plane-wave PBE result. These initial tests indicate that the comparatively inexpensive DFT-based SIMOMM optimizations can provide accuracies comparable to large-basis MP2 calculations.

Solid-state geometries used in the remainder of this work were optimized using SIMOMM employing the UMP2/CCD QM method and the parameters given in Table II. Convergence tests were also performed on 3C-SiC, where improved convergence behavior was noted as compared with 4H-SiC. For the comparatively anisotropic 6H-SiC lattice, we used the largest affordable roughly-cubic supercell, having dimensions $9 \times 9 \times 1.4$. The 3C, 4H, and 6H polytypes make an interesting case study for testing our methods, since there is varying degree

of anisotropy of the unit cells with little other significant change in the environment of the defect.

B. Charge and multiplicity of the ground state

A major challenge in the study of solid-state defects and their photoluminescence spectra, assuming knowledge of the material's polytype and the defect type, is the characterization of the electronic ground state of the defect site in terms of its charge and multiplicity. One consequence of the high symmetry of point defects is orbital degeneracy, and, in analogy to Hund's rule for atoms, this can lead to unusual charges and multiplicities being the most energetically favorable. Energy-ordering states related by incremental changes in charge and multiplicity can be problematic using electronic structure methods such as DFT and TD-DFT because they typically treat

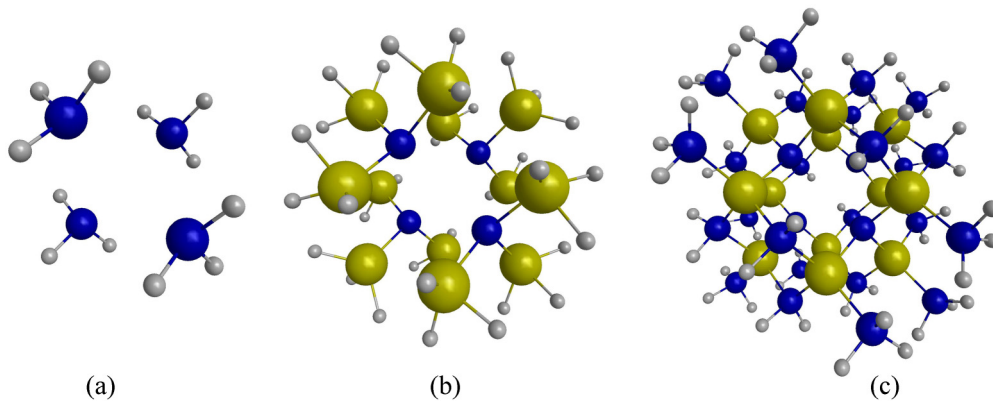


FIG. 3. Atomic configurations of the QM models corresponding to the C₄H₁₂ (a), C₄Si₁₂H₃₆ (b), and C₄₀Si₁₂H₁₂₀ h-center V_{Si}^- defect in 4H-SiC. Carbon atoms are blue, silicon atoms are gold, and hydrogen atoms are gray.

TABLE II. Parameters defining the computational models.

| | SiC polytype | | |
|------------------------|-----------------------|-----------------------|-------------------------|
| | 3C | 4H | 6H |
| space group | F43m | P63mc | P63mc |
| $a(\text{\AA})$ | 4.368 | 3.079 | 3.079 |
| $c(\text{\AA})$ | | 10.07 | 15.12 |
| supercell boundaries | $4 \times 4 \times 4$ | $8 \times 8 \times 2$ | $9 \times 9 \times 1.4$ |
| MM crystal atoms | 865 | 1561 | 1824 |
| MM hydrogen atoms | 539 | 955 | 1007 |
| unique Si-defect sites | 1 | 2 | 3 |
| QM crystal atoms | 4 | 4 | 4 |
| QM hydrogen atoms | 12 | 12 | 12 |

each case with a different SCF reference. Ideally, a method should instead build a series of states from the same correlated reference, as can be done using the EOMCC family of methods. When the appropriate levels of correlation effects are included, these methods will provide a highly accurate description of energy differences between various potential ground states.

Several possible 3C-SiC V_{Si} ground states are illustrated in Fig. 1, where they are represented qualitatively using independent-particle-model orbital energy levels. By now there is consensus that the two most stable electronic configurations are the neutral $S = 1$ state [$V_{\text{Si}}^0(^3A_2)$] and the anionic $S = \frac{3}{2}$ state [$V_{\text{Si}}^-(^4A_2)$], with the latter being the ground state for all three SiC polytypes. Less is known about the relative energies of other states, e.g., $V_{\text{Si}}^0(^1A_1)$, $V_{\text{Si}}^{2-}(^1A_1)$, or $V_{\text{Si}}^-(^2E)$. Since the $V_{\text{Si}}^0(^3A_2)$ species spontaneously ionizes to form the $V_{\text{Si}}^-(^4A_2)$ species, it must be that the additional stabilizing exchange energy produced in the anionic form is greater than the energy gained by breaking the symmetry of the t_2 orbital to form its $5e$ and $14a_1$ components.

Figure 4 plots relative energies of several low-lying 3C-SiC V_{Si} states as a function of basis set size using the UB3LYP, UM11, EA-EOMCCSD, and EA-EOMCCSDt{3} methods. Let us first consider these results in terms of what is known. All combinations of method and basis set correctly place the $^3V_{\text{Si}}^0$ state below the $^1V_{\text{Si}}^0$ state, but there is great variation in the quantitative difference. Beyond this, the ACCD basis set results for the UB3LYP, UM11, and EA-EOMCCSDt{3} methods also correctly place the $^4V_{\text{Si}}^-$ state lowest. Considering the remaining states, it is seen that the energy ordering provided by the DFT and EA-EOMCCSDt{3} methods differ qualitatively and further discussion is warranted.

One potentially consequential discrepancy between the DFT and EA-EOMCCSDt{3} state orderings is their relative placement of the anionic $V_{\text{Si}}^-(^2E)$ state with respect to the neutral $V_{\text{Si}}^0(^3A_2)$ and $V_{\text{Si}}^0(^1A_1)$ states. Limiting the discussion to the ACCD basis set results in Fig. 4, the DFT methods place both anionic states lower than the neutral states, while the EA-EOMCCSDt{3} method places the $V_{\text{Si}}^-(^2E)$ state more than 2 eV higher than the $V_{\text{Si}}^-(^4A_2)$ state, and, importantly, also above both neutral states. Experimental realization of a Lambda system such as the one proposed in Ref. [8] based on DFT calculations, may be compromised by the possibility of system ionization during excitation or relaxation processes occurring between the $V_{\text{Si}}^-(^2E)$ and $V_{\text{Si}}^-(^4A_2)$ states.

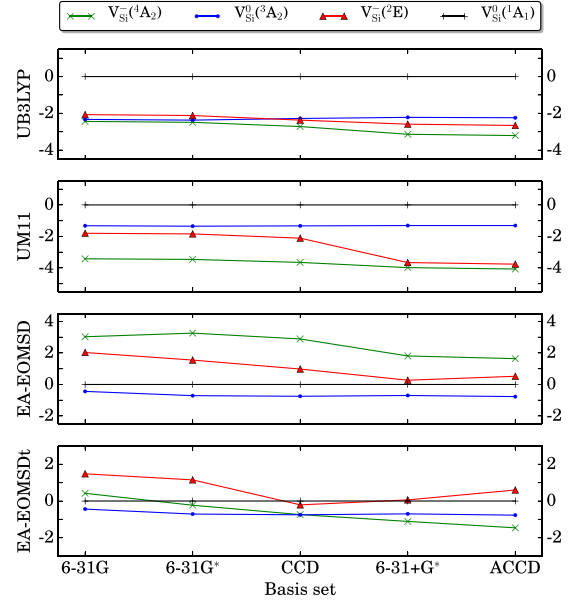


FIG. 4. Relative energies (in eV) of various electronic states of V_{Si} in 3C-SiC. Each value is computed using the designated method and basis set and reported with respect to the corresponding $V_{\text{Si}}^0(^1A_1)$ energy.

Returning to comment on the basis-set dependence of the computational models, all methods presented in Fig. 4 show a significant (>1 eV) shift in at least one of the reported states when going from the 6-31G* to 6-31+G* basis sets. This demonstrates the importance of diffuse functions for the accurate energy ordering of defect states. Both the UB3LYP and EA-EOMCCSDt methods exhibit a basis-set dependence of the state ordering, with the EA-EOMCCSDt state ordering not completely resolved until the ACCD basis set is employed. It is thus important to use good-quality basis sets with diffuse functions when performing energy-ordering studies on minimal vacancy defect models.

Without benchmark values for comparison, it is difficult to draw definitive conclusions from the data in Fig. 4 about the relative accuracy of these methods. Table III provides a quantitative comparison of computed energy differences for the $V_k^0(^1A_1) \rightarrow V_k^-(^4A_1)$ transition, with a literature plane-wave-based GW-approximation value also included for comparison [34]. The UB3LYP and UM11 DFT approaches produce relative energies over twice as large as the GW approximation, while the EA-EOMCCSD method consistently produces the wrong sign for the energy difference. The EA-EOMCCSDt{3} method fares much better. When the ACCD and ACCT basis sets are employed, EA-EOMCCSDt{3} produces values differing by only ~ 0.1 eV from the GW approximation. This provides supportive evidence that the EA-EOMCCSDt{3} produces the most accurate relative energetics of the four methods used here, and thus it likely also provides the most reliable state ordering in Fig. 4.

C. Basis set convergence of excitation energies

In this section we investigate the accuracy and basis-set convergence of excitation energies produced out of the $V_k^-(^4A_1)$

TABLE III. Relative energies (in eV) for the $V_k^0(^1A_1) \rightarrow V_k^-(^4A_1)$ transition, computed using various method and basis-set combinations.

| UB3LYP | UM11 | EA-EOMCCSD | | | | | | EA-EOMCCSDt{3} | | | | | | GW approx. ^a plane-wave |
|--------|-------|------------|--------|------|---------|------|--|----------------|--------|-------|---------|-------|-------|---------------------------------------|
| | | 6-31G | 6-31G* | CCD | 6-31+G* | ACCD | | 6-31G | 6-31G* | CCD | 6-31+G* | ACCD | ACCT | |
| ACCT | ACCT | | | | | | | | | | | | | |
| -3.28 | -4.07 | 3.03 | 3.26 | 2.89 | 1.81 | 1.64 | | 0.42 | -0.24 | -0.75 | -1.11 | -1.46 | -1.67 | -1.58 |

^aReference [34]. Literature computational values were obtained using the *GW* approximation.

state using EOMCC and TD-DFT methods. In Ref. [8] plane-wave DFT calculations were used to qualitatively order a series of doublet and quartet excited states, with symmetries predicted using a purely group-theoretic approach. It is thus an interesting question whether our Gaussian-based procedure will produce energy ordering of excited states similar to the plane-wave DFT calculations. Before making such comparisons, in this section we establish an appropriate method and basis set for our approach through convergence tests.

Table IV collects excitation energies generated using various methods and basis sets, with only the two lowest-lying quartet states, 1^4A_1 and 1^4E , reported. In terms of the basis set convergence, it is clear from Table IV that, regardless of the method, diffuse functions are essential to the accuracy of the model. When the 6-31+G* and ACCD basis sets including diffuse functions are employed, the resulting excitation energies are within 0.25 eV of the corresponding ACCT results, providing a practical alternative to ACCT in defect calculations where expense is a limiting factor. Full IP- and EA-EOMCCSDT results are also included for the 6-31G basis set; the strong similarity of the values produced by the active-space methods and their parent methods (within 0.01 eV) indicates that the active-space orbitals are an appropriate set for capturing the most important triples effects.

Considering more closely the $X^4A_1 \rightarrow 1^4A_1$ transition, in Table IV a significant discrepancy is found between the

excitation energies produced by the UB3LYP, EA-EOMCCSD, and EA-EOMCCSDt{3} methods. Differences between EA-EOMCCSD and EA-EOMCCSDt are attributable to the significant contributions from $r_{\mu,3p-2h}$ amplitudes [see Eqs. (4) and (5)] found for the X^4A_1 state. The EA-EOMCCSDt{3} and UB3LYP methods are also in disagreement for the same transition by nearly 1.0 eV. The EA-EOMCCSDt{3} method places the 1^4A_1 state 1.4 eV higher in energy than the 1^4E state, while UB3LYP predicts the two excited states to be quasidegenerate. Since a well-known deficiency of TD-DFT is that it does not incorporate two-electron transitions, this can again be attributed to the significant $r_{\mu,3p-2h}$ amplitudes appearing in the EA-EOMCCSDt{3} calculations, which indicate that the excitation is not a pure one-electron transition. Indeed, the UB3LYP 1^4A_1 configuration state function is dominated by one large (>0.98) amplitude out of the X^4A_1 state with all other amplitudes being small (<0.1), indicating that there are virtually no accompanying orbital rotations.

Table IV also includes IP-EOMCC results, as these are often more accurate than the EA-EOMCC methods if the target radical anionic ($N+1$)-electron wave function more closely resembles a doubly anionic ($N+2$)-electron species rather than the N -electron one. The EA-EOMCCSDt{3} and IP-EOMCCSDt{6} results converge toward a similar value for the 1^4A_1 state, but the IP-EOMCCSD and IP-EOMCCSDt{6} results do not converge systematically for the $X^4A_1 \rightarrow 1^4E$ transition. In other situations the IP-EOMCC methods may be a better choice, but since the EA-EOMCC methods are a more convenient and accurate choice for these systems we focus on them here for the remainder of this study.

D. Benchmarking excitation energies of silicon-vacancy defects in 4H- and 6H-SiC

Photoluminescence spectra have previously been obtained for 4H- and 6H-SiC, and these can be used to benchmark the accuracy of our approach, which so far has been tested only on 3C-SiC. In Table V excitation energies computed with the UB3LYP/ACCT and EA-EOMCCSDt{3}/ACCD methods are compared with related photoluminescence measurements for all V_{Si}^- defect types in 4H- and 6H-SiC. The EA-EOMCCSDt{3} computational values for the $X^4A_1 \rightarrow 1^2E$ transition are all within 0.1 eV of measurements. The EA-EOMCCSDt{3} energy ordering of different defect types within a given polytype also qualitatively matches with measurements, indicating this method may be helpful in future studies for distinguishing defect types differing subtly in energy. For both the 4H and 6H polytypes the $X^4A_1 \rightarrow 1^4A_1$ transition is nearly 3 eV, which supports the similar assignment made for 3C-SiC in Table IV. We note that the magnitude of the error increases with increasing unit-cell anisotropy, and thus the larger errors found for 6H-SiC would likely be reduced

TABLE IV. Convergence of 3C-SiC excitation energies (in eV) for vertical transitions from the $V_{Si}^{-1}(X^4A_1)$ ground state to the excited 4A_1 state (above) and 4E state (below), corresponding to orbital transitions dominated by $14a_1 \rightarrow 15a_1$ and $14a_1 \rightarrow 6e$ character, respectively [Fig. 1(a)].

| Method | Basis set | | | | | |
|-------------|-----------|--------|------|---------|------|------|
| | 6-31G | 6-31G* | CCD | 6-31+G* | ACCD | ACCT |
| UB3LYP | 2.50 | 2.48 | 2.35 | 1.89 | 1.81 | 1.76 |
| IP-EOMCCSD | 7.56 | 7.33 | 6.44 | 3.85 | 2.49 | 2.62 |
| IP-EOMCCSDt | 7.61 | 6.10 | 5.07 | 2.97 | 2.88 | 2.91 |
| IP-EOMCCSDT | 5.78 | | | | | |
| EA-EOMCCSD | 2.66 | 2.60 | 2.22 | 0.82 | 0.48 | 0.31 |
| EA-EOMCCSDt | 2.60 | 2.56 | 2.43 | 3.00 | 2.94 | 2.75 |
| EA-EOMCCSDT | 2.60 | | | | | |
| UB3LYP | 2.51 | 2.47 | 2.34 | 1.88 | 1.80 | 1.76 |
| IP-EOMCCSD | 2.44 | 2.37 | 2.29 | 1.96 | 3.27 | 3.27 |
| IP-EOMCCSDt | 2.54 | 2.47 | 2.34 | 1.79 | 3.47 | 3.36 |
| IP-EOMCCSDT | 2.54 | | | | | |
| EA-EOMCCSD | 3.04 | 3.09 | 2.23 | 0.22 | 0.06 | 0.14 |
| EA-EOMCCSDt | 3.74 | 4.09 | 3.34 | 1.38 | 1.32 | 1.35 |
| EA-EOMCCSDT | 3.73 | | | | | |

TABLE V. Comparison of computed and measured vertical excitation energies (in eV) for transitions out of the $V_{\text{Si}}^-(^4A_1)$ state in 4H- and 6H-SiC. The upper and lower tables differ only in the computational method used to generate vertical excitation energies, as indicated, while the final line provides measured values for reference.

| UB3LYP/ACCT | | | | | |
|--------------------------|--------|-------|--------|-------|--------|
| State | 4H-SiC | | 6H-SiC | | |
| | k(V1) | h(V2) | k1(V1) | h(V2) | k2(V3) |
| $V_{\text{Si}}^-(^4A_1)$ | 1.990 | 1.513 | 2.051 | 1.754 | 1.218 |
| $V_{\text{Si}}(^1^4E)$ | 1.982 | 1.497 | 2.051 | 1.754 | 0.061 |
| EA-EOMCCSDt/ACCD | | | | | |
| State | 4H-SiC | | 6H-SiC | | |
| | k(V1) | h(V2) | k1(V1) | h(V2) | k2(V3) |
| $V_{\text{Si}}^-(^4A_1)$ | 2.968 | 3.084 | 2.966 | 2.967 | 2.961 |
| $V_{\text{Si}}(^1^4E)$ | 1.424 | 1.321 | 1.334 | 1.331 | 1.329 |
| Experiment ^a | 1.438 | 1.352 | 1.433 | 1.398 | 1.368 |

^aPhotoluminescence measurements of the $X^4A_1 \rightarrow ^1^4E$ transition taken from Refs. [95] and [67].

by utilizing a more complete supercell during the SIMOMM optimization.

Comparing instead the TD-DFT calculations with the measured values, somewhat erratic UB3LYP results were found for the same set of geometries. In more than one case the energies are too large by over 0.5 eV when compared to the corresponding benchmark values, and in almost all cases the $^1^4A_1$ and $^1^4E$ states lie very close in energy, similar to what was found for 3C-SiC in Sec. IV C. For the k2-type 6H-SiC defect, where the $X^4A_1 \rightarrow ^1^4A_1$ excitation energy is too small by more than 1 eV, the underlying DFT calculation has presumably converged to the $^1^4A_1$ state, as evidenced by it being nearly degenerate with the $^1^4E$ state. Since our goal was simply to identify the most accurate methods for our procedure, we did not attempt to rotate the KS orbitals in pursuit of a lower-energy state.

E. Chromium silicon-substitutional defects in SiC

Photoluminescence frequencies of the V_{Si}^- defect are unsuitable for leveraging existing telecommunication technology, and there is consequently ramping interest in screening transition-metal defects for a color center with an emission frequency compatible with fiber-optic technology. While many methods struggle to accurately describe transition-metal excitation energies, the active-space EA- and IP-EOMCC methods have recently proven to be very successful for transition metals when used appropriately [96]. As a more challenging test of our approach, here we make a first attempt at reproducing the excitation energy for a transition-metal defect in SiC. The photoluminescence spectra for a single chromium defect in SiC has been recently measured, and the authors of Ref. [27] have reported peaks at 1.1587 and 1.1898 eV $^3\text{Cr}^{4+}$ defect corresponding to the h - and k -type silicon sites of 4H-SiC, respectively.

After obtaining a converged quartet $\text{Cr}^{3+}(\text{CH}_3)_4$ geometry for 3C-SiC, as described in Sec. III, the preferred charge

TABLE VI. Relative energies of chromium-defect states of incremental charge and multiplicity. Energies were computed using the EE-EOMCCSD/ACCD and EA-EOMCCSDt/ACCD method for systems with an even and odd numbers of electrons, respectively. All values are reported relative to the neutral singlet $\text{Cr}_{\text{Si}}^0(^1A_1)$ state, in eV.

| Species(state) | 6-31G | 6-31+G* | ACCD |
|-------------------------------------|-------|------------------|------------------|
| $\text{Cr}_{\text{Si}}^{2-}(^1A_1)$ | 6.92 | 4.04 | N/C |
| $\text{Cr}_{\text{Si}}^{--}(^2E)$ | 0.11 | -0.49 | 0.27 |
| $\text{Cr}_{\text{Si}}^0(^3A_2)$ | -1.37 | -1.24 | -1.15 |
| $\text{Cr}_{\text{Si}}^{+}(^2E)$ | 4.86 | 5.24 | 5.49 |
| $\text{Cr}_{\text{Si}}^{+}(^4E)$ | 6.97 | 7.47 | 7.81 |
| $\text{Cr}_{\text{Si}}^{2+}(^1A_1)$ | 19.01 | 19.39 | 19.63 |
| $\text{Cr}_{\text{Si}}^{2+}(^3A_2)$ | 19.27 | 19.77 | 20.03 |
| $\text{Cr}_{\text{Si}}^{3+}(^2E)$ | 38.55 | N/C ^a | N/C ^a |
| $\text{Cr}_{\text{Si}}^{4+}(^1A_1)$ | 65.07 | N/C ^a | N/C ^a |
| $\text{Cr}_{\text{Si}}^{4+}(^3A_2)$ | 64.40 | N/C ^a | N/C ^a |

^aThe calculation did not converge.

and multiplicity of the ground state was investigated using EE-EOMCCSD and EA-EOMCCSDt calculations. Our initial exploratory calculations were performed using the 3C polytype of SiC because we encountered convergence problems for Cr-embedded 4H-SiC. From the results presented in Table VI it can be seen that calculations performed at all reported basis set levels place the $\text{Cr}_{\text{Si}}^0(^3A_2)$ species lowest in energy. In this case there is no change in the energy ordering of states with increasing basis set, and, as in Sec. IV B, ground-state energy differences computed using the ACCD basis set appear adequately converged. This agrees with the ground-state multiplicity predicted in Ref. [27].

In Ref. [27] the authors posited that the observed 4H-SiC Cr_{Si}^0 transition is due to a $X^3A_2 \rightarrow ^1^1A_1$ transition. Our 3C-SiC result for that transition is 1.15 eV, in good agreement with the measured 4H-SiC values. Of further interest are the result of our calculation for the 3C-SiC $\text{Cr}_{\text{Si}}^0 X^3A_2 \rightarrow ^1^3A_2$ transition, which yielded a value of 1.44 eV. This transition is close enough to the fiberoptic C band that it may be worth further consideration, especially since these defects can already be reliably created and measured.

V. CONCLUSIONS

In this study we proposed and validated an *ab initio* Gaussian-based method for predicting the structure and excitation spectra of deep-center defects in semiconductors. The procedure is as follows: **Starting from perfect crystalline lattice coordinates, the defect is introduced and the positions of the surrounding atoms are optimized using the QM/MM method SIMOMM. Excitation energies are then computed by applying highly-accurate EOMCC-based methods to a model structure consisting of several atoms immediately adjacent to the defect, in their SIMOMM-optimized positions.** While these minimal model geometries were sufficient to produce excitation energies comparable to the corresponding photoluminescence measurements, it should also be emphasized that the steep

expense of EOMCC methods are being overcome, both through massively parallel computing algorithms and orbital localization schemes. After breaking free of the associated intractable computational scalings, the systematically improvable nature inherent to our SIMOMM-based method will be a critical advantage over plane-wave methods.

It was demonstrated through convergence tests that the Gaussian-based QM/MM method SIMOMM could achieve a similar level of accuracy to plane-wave based PBE calculations using around 1000 atoms in the bulk MM model. With the QM portion sufficiently constrained, and assuming that an adequately large basis set was employed, both MP2 and DFT with the M11 functional were shown to provide accurate geometries with a QM treatment of only the four carbon atoms immediately adjacent to the defect center. Given as a starting point these accurate optimized geometries, EOMCC-based methods were shown to be powerful tools for the prediction of the electronic structure of defect centers. Using a sufficiently large basis set, the EA-EOMCCSDt method reliably predicted the ground state for silicon-vacancy defects among several states varying in charge and multiplicity, and it produced quantitative excitation energies, always in agreement with photoluminescence measurements to within 0.1 eV.

After establishing the accuracy of this procedure on silicon-vacancies in SiC, a first attempt was made to apply it to a chromium silicon-substitutional defect and EOMCC-based methods were successful there too. For 3C-SiC, EE-EOM-CCSD was able to correctly predict a triplet ground state and a related excitation energy closely comparable to the recently measured 4H-SiC photoluminescence spectrum.

The computational procedure developed here will facilitate efficient screening of defect emission frequencies that would otherwise take years to create and measure in the laboratory. This method is broadly applicable to various defects in SiC and other semiconductors, and we will use it in a subsequent study to screen many candidate defects, including transition-metal substitutional defects other than Cr, in pursuit of one that emits in a region compatible with the existing fiber-optic infrastructure. Fabrication of such a device would go a long way toward establishing the silicon-photonics route as the leading candidate platform for the realization of quantum information networks.

ACKNOWLEDGMENTS

The views expressed in this work are those of the authors and do not reflect the official policy or position of the United States Air Force, Department of Defense, or the United States Government. The DoD High Performance Computing Modernization (HPCMO) Program and the AFRL Supercomputing Resource Center (DSRC) are gratefully acknowledged for financial resources and computer time and helpful support. This work was sponsored by a HASI grant from HPCMO (FA8650-17-1-5401) and a joint AFRL/AFIT grant awarded at the AFRL Director's authority managed by Dr. Luke Bissel. This project was enabled in part by an appointment to the Internship/Research Participation Program at the Air Force Institute of Technology, administered by the Oak Ridge Institute for Science and Education through an interagency agreement between the US Department of Energy and AFIT. The authors also thank Dr. Mike Schmidt for help modifying the coupled cluster codes.

- [1] N. Neumann, F. Mizuochi, P. Rempp, H. Hemmer, S. Watanabe, S. Yamasaki, V. Jacques, T. Gaebel, F. Jelezko, and J. Wrachtrup, *Science* **320**, 1326 (2008).
- [2] M. W. Doherty, N. B. Manson, P. Delany, F. Jelezko, J. Wrachtrup, and L. C. L. Hollenberg, *Phys. Rep.* **528**, 1 (2013).
- [3] S. Castelletto, B. C. Johnson, V. Ivády, N. Stavrias, T. Umeda, A. Gali, and T. Ohshima, *Nat. Mater.* **13**, 151 (2014).
- [4] D. J. Christle, A. L. Falk, P. Andrich, P. V. Klimov, J. U. Hassan, N. T. Son, E. Janzén, T. Ohshima, and D. D. Awschalom, *Nat. Mater.* **14**, 160 (2015).
- [5] M. Widmann, S.-Y. Lee, T. Rendler, N. T. Son, H. Fedder, S. Paik, L.-P. Yang, N. Zhao, S. Yang, I. Booker, A. Denisenko, M. Jamali, S. A. Momenzadeh, I. Gerhardt, T. Ohshima, A. Gali, E. Janzén, and J. Wrachtrup, *Nat. Mater.* **14**, 164 (2015).
- [6] I. Aharonovich, D. Englund, and M. Toth, *Nat. Photonics* **10**, 631 (2016).
- [7] X. He, N. F. Hartmann, X. Ma, Y. Kim, R. Ihly, J. L. Blackburn, W. Gau, J. Kono, Y. Yomogida, A. Hirano, T. Tanaka, H. Kataura, H. Htoon, and S. K. Doorn, *Nat. Photonics* **11**, 577 (2017).
- [8] Ö. O. Soykal, P. Dev, and S. E. Economou, *Phys. Rev. B* **93**, 081207 (2016).
- [9] C. Bradac, T. Gaebel, N. Naidoo, M. J. Sellars, J. Twamley, L. J. Brown, A. S. Barnard, T. Plakhotnik, A. V. Zvyagin, and J. R. Rabeau, *Nat. Nanotechnol.* **5**, 345 (2010).
- [10] M. W. Doherty, F. Dolde, H. Fedder, F. Jelezko, J. Wrachtrup, N. B. Manson, and L. C. L. Hollenberg, *Phys. Rev. B* **85**, 205203 (2012).
- [11] A. O. Levchenko, V. V. Vasil'ev, S. A. Zibrov, A. S. Zibrov, A. V. Sivak, and I. V. Fedotov, *Appl. Phys. Lett.* **106**, 102402 (2015).
- [12] J. Steeds, G. Evans, L. Danks, and S. Furkert, *Diamond Relat. Mater.* **11**, 1923 (2002).
- [13] J. Wang, X. Zhang, Y. Zhou, K. Li, Z. Wang, P. Peddibhotla, F. Liu, S. Bauerdick, A. Rudzinski, Z. Liu, and W. Gao, *ACS Photonics* **4**, 1054 (2017).
- [14] J. Wang, Y. Zhou, X. Zhang, F. Liu, Y. Li, K. Li, Z. Liu, G. Wang, and W. Gao, *Phys. Rev. Appl.* **7**, 064021 (2017).
- [15] M. Radulski, M. Widmann, M. Niethammer, J. L. Zhang, S.-Y. Lee, T. Rendler, K. G. Lagoudakis, N. T. Son, E. Janzén, T. Ohshima, J. Wrachtrup, and J. Vučković, *Nano Lett.* **17**, 1782 (2017).
- [16] T. Kimoto and J. A. Cooper, *Fundamentals of Silicon Carbide Technology: Growth, Characterization, Devices, and Applications* (Wiley, Singapore, 2014), pp. 11–38.
- [17] A. L. Falk, B. B. Buckley, G. Calusine, W. F. Koehl, V. V. Dobrovitski, A. Politi, C. A. Zorman, P. X.-L. Feng, and D. D. Awschalom, *Nat. Comm.* **4**, 1819 (2013).
- [18] K. Horowitz, T. Remo, and S. Reese, A Manufacturing Cost and Supply Chain Analysis of SiC Power Electronics Applicable to Medium-Voltage Motor Drives, Technical Report TP-6A20-67694 (National Renewable Energy Laboratory, 2017).
- [19] L. Wang, Q. Cheng, H. Qin, Z. Li, Z. Lou, J. Lu, J. Zhang, and Q. Zhou, *Dalton Trans.* **46**, 2756 (2017).
- [20] R. Nagy, M. Widmann, M. Niethammer, D. B. R. Dasari, I. Gerhardt, Ö. O. Soykal, M. Radulski, T. Ohshima, J. Vučković,

- N. T. Son, I. G. Ivanov, S. E. Economou, C. Bonato, S.-Y. Lee, and J. Wrachtrup, [arXiv:1707.02715](#) [Phys. Rev. Appl. (to be published)].
- [21] F. Olbricha, J. Höschle, M. Müller, J. Kettler, S. L. Portalupi, M. Paul, M. Jetter, and P. Michler, *Appl. Phys. Lett.* **111**, 133106 (2017).
- [22] H. Seo, A. L. Falk, P. V. Kilmov, K. C. Miao, G. Galli, and D. D. Awschalom, *Nat. Comm.* **7**, 12935 (2017).
- [23] A. Csóré, H. J. von Bardeleben, J. L. Cantin, and A. Gali, *Phys. Rev. B* **96**, 085204 (2017).
- [24] H. J. von Bardeleben and J. L. Cantin, *MRS Commun.* **7**, 591 (2017).
- [25] T. Umeda, N. T. Son, J. Isoya, E. Janzén, T. Ohshima, N. Morishita, H. Itoh, A. Gali, and M. Bockstedte, *Phys. Rev. Lett.* **96**, 145501 (2006).
- [26] K. Szász, V. Ivády, I. A. Abrikosov, E. Janzén, M. Bockstedte, and A. Gali, *Phys. Rev. B* **91**, 121201 (2015).
- [27] W. F. Koehl, B. Diler, S. J. Whiteley, A. Bourassa, N. T. Son, E. Janzén, and D. D. Awschalom, *Phys. Rev. B* **95**, 035207 (2017).
- [28] M. A. L. Marques and E. K. U. Gross, *Annu. Rev. Phys. Chem.* **55**, 427 (2004).
- [29] A. Dreuw and M. Head-Gordon, *Chem. Rev.* **105**, 4009 (2005).
- [30] A. D. Laurent and D. Jacquemin, *Int. J. Quantum Chem.* **113**, 2019 (2013).
- [31] C. Adamo and D. Jacquemin, *Chemical Society Reviews* **42**, 845 (2013).
- [32] N. T. Maitra, *J. Phys.: Condens. Matter* **28**, 423001 (2017).
- [33] F. Aryasetiawan and O. Gunnarsson, *Rep. Prog. Phys.* **61**, 237 (1998).
- [34] F. Bruneval and G. Roma, *Phys. Rev. B* **83**, 144116 (2011).
- [35] G. H. Booth, A. Grüneis, G. Kresse, and A. Alavi, *Nature (London)* **493**, 365 (2013).
- [36] K. Liao and A. Grüneis, *J. Chem. Phys.* **145**, 141102 (2016).
- [37] F. Hummel, T. Tsatsoulis, and A. Grüneis, *J. Chem. Phys.* **146**, 124105 (2017).
- [38] J. A. Krmhansl, *Localized Excitations in Solids*, edited by R. F. Wallis (Springer, New York, 1968), p. 17.
- [39] J. R. Shoemaker, L. W. Burggraf, and M. S. Gordon, *J. Phys. Chem. A* **103**, 3245 (1999).
- [40] F. Maseras and K. Morokuma, *J. Comput. Chem.* **16**, 1170 (1995).
- [41] C. H. Choi and M. S. Gordon, *J. Am. Chem. Soc.* **121**, 11311 (1999).
- [42] G. M. Li, L. W. Burggraf, J. R. Shoemaker, D. Eastwood, and A. E. Stigman, *Appl. Phys. Lett.* **76**, 3373 (2000).
- [43] Y. S. Jung, C. H. Choi, and M. S. Gordon, *J. Phys. Chem. B* **105**, 4039 (2001).
- [44] C. H. Choi and M. S. Gordon, *J. Am. Chem. Soc.* **124**, 6162 (2002).
- [45] C. H. Choi, D. J. Liu, J. W. Evans, and M. S. Gordon, *J. Am. Chem. Soc.* **124**, 8730 (2002).
- [46] H. Tamura and M. S. Gordon, *J. Chem. Phys.* **119**, 10318 (2003).
- [47] J. M. Rintelman and M. S. Gordon, *J. Phys. Chem. B* **108**, 7820 (2004).
- [48] Y. S. Jung and M. S. Gordon, *J. Am. Chem. Soc.* **127**, 3131 (2005).
- [49] H. S. Lee, C. H. Choi, and M. S. Gordon, *J. Phys. Chem. B* **109**, 5067 (2005).
- [50] H. S. Lee, C. H. Choi, and M. S. Gordon, *J. Am. Chem. Soc.* **127**, 8485 (2005).
- [51] J. J. Lutz and J. M. Hutson, *J. Mol. Spectrosc.* **330**, 43 (2016).
- [52] A. A. Sokol, S. T. Bromley, S. A. French, C. R. A. Catlow, and P. Sherwood, *Int. J. Quantum Chem.* **99**, 695 (2003).
- [53] N. Choly, G. Lu, W. E, and E. Kaxiras, *Phys. Rev. B* **71**, 094101 (2005).
- [54] Y. Liu, G. Lu, Z. Chen, and N. Kioussis, *Modelling Simul. Mater. Sci. Eng.* **15**, 275 (2007).
- [55] M. Nooijen and R. J. Bartlett, *J. Chem. Phys.* **102**, 3629 (1995).
- [56] M. Nooijen and R. J. Bartlett, *J. Chem. Phys.* **102**, 6735 (1995).
- [57] N. Oliphant and L. Adamowicz, *J. Chem. Phys.* **94**, 1229 (1991).
- [58] N. Oliphant and L. Adamowicz, *J. Chem. Phys.* **96**, 3739 (1992).
- [59] N. Oliphant and L. Adamowicz, *Int. Rev. Phys. Chem.* **12**, 339 (1993).
- [60] P. Piecuch, N. Oliphant, and L. Adamowicz, *J. Chem. Phys.* **99**, 1875 (1993).
- [61] J. R. Gour, P. Piecuch, and M. Włoch, *J. Chem. Phys.* **123**, 134113 (2005).
- [62] J. R. Gour and P. Piecuch, *J. Chem. Phys.* **125**, 234107 (2006).
- [63] J. A. Hansen, P. Piecuch, J. J. Lutz, and J. R. Gour, *Phys. Scr.* **84**, 028110 (2011).
- [64] M. Ehara, P. Piecuch, J. J. Lutz, and J. R. Gour, *Chem. Phys.* **399**, 94 (2012).
- [65] J. N. Byrd, J. J. Lutz, Y. Jin, D. S. Ranasinghe, J. A. Montgomery, Jr., A. Perera, X. F. Duan, L. W. Burggraf, B. A. Sanders, and R. J. Bartlett, *J. Chem. Phys.* **145**, 024312 (2016).
- [66] J. J. Lutz, X. F. Duan, D. S. Ranasinghe, Y. Jin, J. T. Margraf, A. Perera, L. W. Burggraf, and R. J. Bartlett (unpublished).
- [67] M. Wagner, B. Magnusson, W. M. Chen, E. Janzén, E. Sörman, C. Hallin, and J. L. Lindström, *Phys. Rev. B* **62**, 16555 (2000).
- [68] J. Schneider and K. Maier, *Physica B* **185**, 199 (1993).
- [69] H. Itoh, A. Kawasuso, T. Ohshima, M. Yoshikawa, I. Nashiyama, S. Tanigawa, S. Misawa, H. Okumura, and S. Yoshida, *Phys. Stat. Sol.* **162**, 173 (1997).
- [70] S. B. Orlinski, J. Schmidt, E. N. Mokhov, and P. G. Baranov, *Phys. Rev. B* **67**, 125207 (2003).
- [71] D. Riedel, F. Fuchs, H. Kraus, S. Văth, A. Sperlich, V. Dyakonov, A. A. Soltamova, P. G. Baranov, V. A. Ilyin, and G. V. Astakhov, *Phys. Rev. Lett.* **109**, 226402 (2012).
- [72] P. Piecuch, *Mol. Phys.* **108**, 2987 (2010).
- [73] K. Momma and F. Izumi, *J. Appl. Crystallogr.* **44**, 1272 (2011).
- [74] M. A. Davis, *J. Org. Chem.* **32**, 1161 (1967).
- [75] M. D. Hanwell, D. E. Curtis, D. C. Lonie, T. Vandermeersch, E. Zurek, and G. R. Hutchison, *J. Cheminform.* **4**, 17 (2012).
- [76] J. W. Ponder and F. M. Richards, *J. Comput. Chem.* **8**, 1016 (1987).
- [77] N. M. O'Boyle, M. Banck, C. A. James, C. Morley, T. Vandermeersch, and G. R. Hutchison, *J. Cheminform.* **3**, 33 (2011).
- [78] M. W. Schmidt, K. K. Baldridge, J. A. Boatz, S. T. Elbert, M. S. Gordon, J. J. Jensen, S. Koseki, N. Matsunaga, K. A. Nguyen, S. Su, T. L. Windus, M. Dupuis, and J. A. Montgomery, Jr., *J. Comput. Chem.* **14**, 1347 (1993).
- [79] M. S. Gordon and M. W. Schmidt, in *Theory and Applications of Computational Chemistry, the First Forty Years*, edited by C. E. Dykstra, G. Frenking, K. S. Kim, and G. E. Scuseria (Elsevier, Amsterdam, 2005), pp. 1167–1189.
- [80] B. M. Bode and M. S. Gordon, *J. Mol. Graphics and Modeling* **16**, 133 (1998).
- [81] C. M. Aikens and M. S. Gordon, *J. Phys. Chem. A* **108**, 3103 (2004).

- [82] F. Fuchs, V. A. Soltamov, S. V  th, P. G. Baranov, E. N. Mokhov, G. V. Astakhov, and V. Dyakonov, *Sci. Rep.* **3**, 1637 (2013).
- [83] J. E. Boyd, Excited states of silicon carbide clusters by time dependent density functional theory, Ph.D. thesis, Air Force Institute of Technology, 2004.
- [84] J. A. Pople, P. M. W. Gill, and N. C. Handy, *Int. J. Quantum Chem.* **56**, 303 (1995).
- [85] J. P. Bowen, V. V. Reddy, D. G. Patterson, Jr., and N. L. Allinger, *J. Org. Chem.* **53**, 5471 (1988).
- [86] P. C. Hariharan and J. A. Pople, *Theoret. Chimica Acta* **28**, 213 (1973).
- [87] M. M. Francl, W. J. Pietro, W. J. Hehre, J. S. Binkley, M. S. Gordon, D. J. DeFrees, and J. A. Pople, *J. Chem. Phys.* **77**, 3654 (1982).
- [88] T. Clark, J. Chandrasekhar, and P. v. R. Schleyer, *J. Comp. Chem.* **4**, 294 (1983).
- [89] R. Krishnam, J. S. Binkley, R. Seeger, and J. A. Pople, *J. Chem. Phys.* **72**, 650 (1980).
- [90] P. M. W. Gill, B. G. Johnson, J. A. Pople, and M. J. Frisch, *Chem. Phys. Lett.* **197**, 499 (1992).
- [91] T. H. Dunning, Jr., *J. Chem. Phys.* **90**, 1007 (1989).
- [92] D. Woon and T. H. Dunning, Jr., *J. Chem. Phys.* **98**, 1358 (1993).
- [93] T. H. Dunning, Jr., K. A. Peterson, and A. K. Wilson, *J. Chem. Phys.* **114**, 9244 (2001).
- [94] J. C. A. Prentice, B. Monserrat, and R. J. Needs, *Phys. Rev. B* **95**, 014108 (2017).
- [95] E. S  rman, N. T. Son, W. M. Chen, O. Kordina, C. Hallin, and E. Janz  n, *Phys. Rev. B* **61**, 2613 (2000).
- [96] N. P. Bauman, J. A. Hansen, and P. Piecuch, *J. Chem. Phys.* **145**, 084306 (2016).